Pure and Applied Geophysics

Rock Physics Modeling and Seismic AVAZ Responses of Fractured Reservoirs with Different Azimuths

JING BA,[1] WEI ZHANG,[1] GUANGTAN HUANG,[2] TOBIAS M. MÜLLER,[1,3] and CONG LUO[1]

Abstract—Fracture orientation and in particular the fracture strike play an important role in guiding the accurate estimation of the orientation of in situ stress fields. Fracture strike can be extracted based on the azimuthal seismic reflection responses. Thus, the characteristics of seismic reflection responses varying with fracture strike are critical for fracture strike estimation. In this work, a set of vertical fractures with different strikes is introduced into an isotropic host matrix based on the Schoenberg linear-slip theory, and the azimuthal seismic reflection response is modeled based on the reflection/transmission analysis at a plane interface. The effect of fracture parameters, i.e., fracture density, fracture aspect ratio, and fluid infill on the seismic reflection response, is analyzed. The influences of fracture strike on the stiffness matrix are simulated, and we further discuss the impacts on the P- and S-wave velocities. The influences of fracture strike on the reflection coefficient are depicted using the rose diagram method. The proposed workflow is applied to real seismic reflection data. The method is used to estimate the fracture strike with the seismic data in the Sichuan Basin work area by assuming that all fractures are vertically oriented, and the rose diagram is obtained close to the target layer. The results show that the fracture strike predicted by the method is in good agreement with the estimation based on the well-bore imaging data.

Keywords: Fracture strike, fracture weakness, stiffness matrix, azimuth, reflection coefficient, rock physics modeling.

1. Introduction

Fracture system is an important factor that affects the production quality of shale reservoirs. They generally play a role in the subsurface storage and transport channels for oil and gas. The accurate prediction of fractures is key and has proved to be a difficult point for shale gas reservoir developments (Li et al., 2018; Lyu et al., 2017; Marfurt et al., 1998). Specifically, the strike of fracture distributions is an important target for seismic detection and exploration. For shale reservoirs, reliable fracture feature descriptions and accurate fracture spatial predictions are helpful for improving efficient hydrocarbon exploration and further optimizing the production and development designs (Gong et al., 2021a, b).

Azimuthal anisotropy in rocks can result from the presence of one or more sets of partially aligned fractures with orientations determined by the stress history of the formation. Thus, the anisotropy of seismic reflection responses can be utilized to estimate the fracture orientation (e.g., Sayers et al., 2001). The model of real strata can be simplified to be anisotropic along a single direction in engineering applications, i.e., transversely isotropy (TI) medium. With the development of fracture detection techniques, fracture strike estimation based on seismic reflection data has attracted increasing attention (Long et al., 2011).

Since the start of the studies on natural fractures of formations in the 1960s, fracture prediction methods have gradually evolved. The presented methods for predicting fractures include post-stack attribute fracture and pre-stack seismic anisotropic fracture predictions. Post-stack seismic attributes are mainly the properties related to the amplitude, frequency, waveforms, and other attributes extracted from post-stack seismic data.

The coherence attribute was proposed by Bahorich and Farmer (1995) to characterize the similarity between adjacent data. It can be used to predict the

[1] School of Earth Sciences and Engineering, Hohai University, Nanjing 211100, China.
[2] Institute of Rock and Soil Mechanics, Chinese Academy of Sciences, Wuhan 430071, Hubei, Province, China. E-mail: huangguangtan1@163.com
[3] Department of Seismology, Centro de Investigación Científica y de Educación Superior de Ensenada, 22860 Ensenada, Mexico.

fracture development zones and macroscopically determine the development and distribution characteristics of fractures. However, the ability to identify fractures is limited. For the zones with developed fractures, Lisle (1994) analyzed the relations between the Gaussian curvature and open fractures measured on an outcrop. The curvature attribute is an indirect indicator to identify the locations of fracture developments. It indirectly and qualitatively describes the development of fractures and reflects the fractures caused by structural deformation. Dorigo (1996) proposed the ant algorithm. Pedersen et al. (2002) proposed a method of fracture identification using ant tracking. Fractures can be effectively predicted and described by retrieving these seismic properties (e.g., the coherence attribute, curvature attribute, and ant-tracking body attribute). However, instead of characterizing fracture distribution characteristics, the aforementioned methods majorly focus on the descriptions of large-scale faults (Marfurt, 2007).

For fracture prediction based on prestack seismic data, the azimuthal anisotropy difference is exploited (Crampin, 1981, 1985; Thomsen, 1986). With the development of amplitude versus offset (AVO) techniques, the amplitude versus angle and azimuth (AVAZ) fracture detection methods have been developed and gradually became important tools in fracture detection technology. Different degrees of fracture development affect the anisotropy in the azimuth properties of reservoir rocks, and this feature can be exploited to identify and predict fractures. AVAZ fracture detection technique can quantitatively reflect the fracture properties of a HTI (horizontal transverse isotropic) medium (Afzal et al., 2022; Liu et al., 2022; Pan et al., 2017).

Fracture characterization is usually based on the concept of an effective medium model. The widely used effective medium theories include the Hudson model (Hudson, 1981) and linear slip model proposed by Schoenberg (1980), which describes the case of a HTI medium with a single set of vertically oriented fractures. According to the approximate formulae of the HTI medium P-wave reflection coefficients, Rüger (1998) inverted the azimuth and azimuth anisotropy terms to predict the fracture direction and development degree of the HTI medium (Schoenberg et al., 1995). Rüger (2002) established the approximate equation of the azimuth AVO reflection coefficients in a HTI medium.

In addition, Li (1999) proposed an approximation for the reflection amplitudes of the HTI fractured media with any azimuth. Mallick et al. (1998) estimated fracture orientation and fracture density according to the ellipse variations of amplitude with azimuth. Al-Marzong et al. (2006) fitted the variations of AVO gradients at different orientations regarding the observed orientation as an ellipse in the polar coordinate system and applied the ellipticity to characterize the development of fracture density. Bacharch et al. (2009) extended the approximate equations of reflection coefficients of a HTI medium to those of an orthotropic medium. For a wide azimuth angle, an AVAZ attribute inversion based on the orthotropic fracture model was performed with pre-stack seismic data for fracture predictions. Downton et al. (2010, 2015) used the Fourier series to expand Ruger's equation of azimuthal AVO reflection coefficient and predicted fractures based on the second-order Fourier coefficients. Based on the pre-stack azimuthal gathers, Yin et al. (2014) developed an anisotropic gradient inversion method to predict fractures. Wang et al. (2021) applied an azimuthal Young's modulus ellipse-fitting to predict fractures. Liu et al. (2018a) performed the AVAZ property analysis and fracture prediction of an orthotropic media for tight oil reservoirs. In the absence of different fracture fluid fillings, the relation between fracture properties and AVAZ responses was analyzed.

In this study, we consider a two-layer model with a single interface, in which the upper layer is an isotropic medium, the lower layer is a HTI medium, and the thickness of each layer is 50 m, to simulate the seismic reflection response of the TI medium with fracture-induced anisotropy, as shown in Fig. 1. The parameters of the upper and lower layer are shown in Table 1 and correspond to typical AVAZ responses.
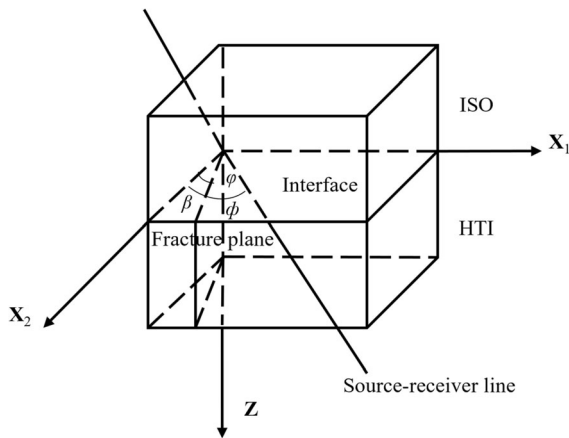
Figure 1
Schematic diagram of the single interface model I

As shown in Fig. 1, x_1, x_2, and z are the coordinate axes in model I, respectively, β denotes the angle between the fracture plane and the x_2 axis, ϕ corresponds to the azimuth angle of the source-receiver line, and $\varphi = \phi - \beta$ is the fracture azimuth angle. Previous studies on the effective compliance matrix mainly focused on the elastic media with fractures parallel or perpendicular to the x_2 axis (Liu et al., 2018b; Pan et al., 2016). Based on model I, we propose a fracture prediction method. It is related to a set of vertical fracture systems with any development direction in the host medium. First, based on the linear slip model as given in Sect. 2.1, a fracture stiffness matrix is constructed. Then, according to the scattering theory as given in Sect. 2.2, the stiffness matrix obtained is combined with the formula of P-wave reflection coefficients of a HTI medium by Shaw and Sen (2004, 2006) to calculate AVAZ reflection coefficients. Finally, according to the results of AVAZ analysis, a rose diagram is proposed, and the fracture azimuth information is estimated with the AVAZ attributes. This is the focus of the

proposed method of fracture prediction. Besides, we have added the analysis of factors affecting fracture weakness, as shown in Sect. 2.3 and 3.1, and the influence of β on the stiffness coefficients and velocities as shown in Sect. 2.4 and 3.2. The fourth part is given to verify the proposed method with the field seismic data of Sichuan Basin work area.

2. Basic Theory

2.1. Establishment of Rock Stiffness Matrix with Vertical Fractures

Schoenberg (1980) proposed a model of an incomplete bonding interface between two elastic media. The displacement discontinuity, or slip, is taken to be linearly related to the stress traction, which is continuous across the interface. For isotropic interface behavior, there are two complex frequency-dependent interface compliances, Z_N and Z_T, where Z_N is the normal compliance, which is perpendicular to the fracture surface, and Z_T is the tangential compliance, which is parallel to the fracture surface.

The effective elastic tensor of the fractured medium (i.e., the sum of the elastic tensor of the host matrix and that of the aligned fracture groups) is related to Z_N and Z_T. For a set of parallel fractures embedded in an isotropic host medium, the linear-slip model can be applied, and the effective medium can be considered as a transversely isotropic model with its horizontal axis of symmetry perpendicular to the fractures. In this elastic medium, the effective compliance matrix can be determined as the sum of the host compliance and the excess fracture compliance due to the presence of fractures (Schoenberg & Sayers, 1995).

Table 1

Parameters of model I

	V_{P0} (km/s)	V_{S0} (km/s)	V_{P90} (km/s)	V_{S90} (km/s)	Density (g/cm^3)	Δ_N	Δ_T	Thickness (m)
ISO	3.410	1.640	3.410	1.640	2.60	0	0	50
HTI	6.640	3.440	6.489	3.549	2.71	0.1291	0.2580	50

According to the Schoenberg model, the stiffness matrix **C** can be derived with the stiffness matrix of the host rock and fracture system (Schoenberg & Sayers, 1995),

$$\mathbf{C} = \mathbf{S}^{-1} = \left(\mathbf{S}_b + \sum_q \mathbf{S}_f^{(q)}\right)^{-1}, \qquad (1)$$

where **S** denotes compliance matrix of the effective medium, $\mathbf{S}_b$ is the compliance of the host medium, $\mathbf{S}_f$ is the compliance of the fracture system, and q is the ordinal number of the fracture system. In the Voigt notation, the stiffness matrix $\mathbf{C}_b$ of the isotropic medium is

$$\mathbf{C}_b = \begin{bmatrix} \lambda+2\mu & \lambda & \lambda & 0 & 0 & 0 \\ \lambda & \lambda+2\mu & \lambda & 0 & 0 & 0 \\ \lambda & \lambda & \lambda+2\mu & 0 & 0 & 0 \\ 0 & 0 & 0 & \mu & 0 & 0 \\ 0 & 0 & 0 & 0 & \mu & 0 \\ 0 & 0 & 0 & 0 & 0 & \mu \end{bmatrix}, \quad (2)$$

where λ and μ denote the first and second Lamé parameters of the host matrix without fractures.

$$\lambda = V_{P0}^2\rho - 2V_{S0}^2\rho, \qquad (3a)$$

$$\mu = V_{S0}^2\rho, \qquad (3b)$$

where V_{P0} and V_{S0} are the P- and S-wave velocities at the vertical direction (although they are independent with wave transmission direction for the isotropic case), respectively, and ρ is density; these are given in Table 1.

Then, the compliance matrix of the host $\mathbf{S}_b$ can be obtained. The development direction of the first q groups of the fracture system is related to $\beta(q)$. The compliance matrix $\mathbf{S}_f$ with a set of fractures is

$$\mathbf{S}_f = \begin{bmatrix} S_{11} & S_{12} & 0 & 0 & 0 & S_{16} \\ S_{12} & S_{22} & 0 & 0 & 0 & S_{26} \\ 0 & 0 & 0 & 0 & 0 & 0 \\ 0 & 0 & 0 & S_{44} & S_{45} & 0 \\ 0 & 0 & 0 & S_{45} & S_{55} & 0 \\ S_{16} & S_{26} & 0 & 0 & 0 & S_{66} \end{bmatrix}, \quad (4)$$

(Schoenberg et al., 1999), and the specific expressions of the components in Eq. (4) are

$$S_{11} = \frac{3Z_N+Z_H}{8} + \frac{Z_N}{2}\cos\beta + \frac{Z_N-Z_H}{8}\cos4\beta, \quad (5a)$$

$$S_{12} = \frac{Z_N-Z_H}{8}(1-\cos4\beta), \qquad (5b)$$

$$S_{16} = \frac{Z_N\sin2\beta}{2} + \frac{Z_N-Z_H}{4}\sin4\beta, \qquad (5c)$$

$$S_{22} = \frac{3Z_N+Z_H}{8} - \frac{Z_N}{2}\cos\beta + \frac{Z_N-Z_H}{8}\cos4\beta, \quad (5d)$$

$$S_{22} = \frac{3Z_N+Z_H}{8} - \frac{Z_N}{2}\cos\beta + \frac{Z_N-Z_H}{8}\cos4\beta, \quad (5e)$$

$$S_{26} = \frac{Z_N\sin2\beta}{2} - \frac{Z_N-Z_H}{4}\sin4\beta, \qquad (5f)$$

$$S_{44} = \frac{Z_V(1-\cos2\beta)}{2}, \qquad (5g)$$

$$S_{45} = \frac{Z_V\sin\beta}{2}, \qquad (5h)$$

$$S_{55} = \frac{Z_V(1+\cos2\beta)}{2}, \qquad (5i)$$

$$S_{66} = \frac{Z_N+Z_H}{2} - \frac{Z_N-Z_H}{2}\cos4\beta, \qquad (5j)$$

where Z_V and Z_H are the vertical and horizontal tangential compliances, respectively. For a HTI media,

$$Z_V = Z_H = Z_T. \qquad (6)$$

Thus, the stiffness matrix **C** of the HTI media containing one groups of different fractures is obtained.

$$\mathbf{C} = \begin{bmatrix} C_{11} & C_{12} & C_{13} & 0 & 0 & C_{16} \\ C_{21} & C_{22} & C_{23} & 0 & 0 & C_{26} \\ C_{31} & C_{32} & C_{33} & 0 & 0 & C_{36} \\ 0 & 0 & 0 & C_{44} & C_{45} & 0 \\ 0 & 0 & 0 & C_{54} & C_{55} & 0 \\ C_{61} & C_{62} & C_{63} & 0 & 0 & C_{66} \end{bmatrix}. \quad (7)$$

2.2. TI Medium Reflection Coefficient Equation

Shaw and Sen (2004, 2006) linearized the P–P wave reflection coefficients in a weakly anisotropic media to characterize the fracture-induced weak anisotropy. By combining the matrix obtained in 2.1 with it, i.e., combining the perturbation matrix with the scattering theory, the PP reflection coefficient can be represented as (Shaw & Sen, 2004, 2006)

$$R_{PP} = \frac{1}{4\rho_b \cos^2\theta}\left(\Delta\rho\xi + \sum_{m=1}^{6}\sum_{n=1}^{6}\Delta C_{mn}\eta_{mn}\right), \quad (8)$$

where $\Delta\rho = \rho_2 - \rho_1$ and $\Delta C = C_2 - C_1$ represent the perturbations of density and stiffness matrices caused by the fracture development, respectively. ρ_1 and ρ_2 represent the densities of the upper and lower media in the two-layer model, respectively. ρ_b represents the density of the host medium, and C_1 and C_2 are the stiffnesses of the upper and lower media, respectively. θ is the incident angle, the two parameters ξ and η are associated with the slowness vector $\mathbf{p}$ and the polarization vectors $\mathbf{t}$. ξ, η, $\mathbf{p}$ and $\mathbf{t}$ are determined as are shown in Appendix A.

2.3. Normal and Tangential Weakness Equations of Fractures

Hsu and Schoenberg (1993) proposed the two dimensionless parameters Δ_N and Δ_T to characterize the changes in rock stiffnesses due to the presence of fractures (Hsu & Schoenberg, 1993):

$$\Delta_N = \frac{(\lambda + 2\mu)Z_N}{1 + (\lambda + 2\mu)Z_N}, \quad (9a)$$

$$\Delta_T = \frac{\mu Z_N}{1 + \mu Z_N}, \quad (9b)$$

where Δ_N represents the variation of elastic parameters induced by fractures in the direction perpendicular to the fracture surface, and Δ_T denotes the variation of elastic parameters induced by fractures in the direction parallel to the fracture surface, which is also called fracture weakness.

Schoenberg and Douma (1988) and Teng (1998) neglected the high-order corrections and considered the first-order correction of the Hudson model (Hudson, 1981) and established the relation between the linear slip model and the Hudson thin coin-shaped model (Hudson, 1981).

$$\Delta_N = \frac{\lambda + 2\mu}{\mu}U_{33}e, \quad (10a)$$

$$\Delta_T = U_{11}e, \quad (10b)$$

where e denotes fracture density, and U_{33} and U_{11} are the coefficients of the Hudson model, which can be determined with

$$U_{11} = \frac{16(\lambda + 2\mu)}{3(3\lambda + 4\mu)}\frac{1}{1 + M}, \quad (11a)$$

$$U_{33} = \frac{4(\lambda + 2\mu)}{3(\lambda + \mu)}\frac{1}{1 + k}, \quad (11b)$$

where M and k are the parameters related to the fracture characteristics (Schoenberg & Douma, 1988).

$$M = \frac{4\mu'(\lambda + 2\mu)}{\pi\chi\mu(\lambda + \mu)}, \quad (12a)$$

$$k = \frac{[K' + (4/3)\mu'](\lambda + 2\mu)}{\pi\chi\mu(\lambda + \mu)}, \quad (12b)$$

$$K' = \rho_f V_{Pf}^2, \quad (13a)$$

$$\mu' = \rho_f V_{Sf}^2, \quad (13b)$$

where K' and μ' are the bulk and shear moduli of fracture fluid, respectively. V_{Pf} and V_{Sf} are P- and S-wave velocities of fluid, respectively. ρ_f is fluid density.

Substituting Eqs. 11(a)–12(b) sinto Eqs. (10a) and 10(b), we have

$$\Delta_N = \frac{4e}{3g(1-g)\left[1 + \frac{1}{\pi(1-g)}\left(\frac{K' + 4/3\mu'}{\mu\chi}\right)\right]}, \quad (14a)$$

$$\Delta_T = \frac{16e}{3(3-2g)\left[1 + \frac{4}{\pi(3-2g)}\left(\frac{\mu'}{\mu\chi}\right)\right]}, \quad (14b)$$

where $g = \mu/(\lambda + 2\mu)$, and χ is fracture aspect ratio.

2.4. Elastic Wave Velocities in TI Medium

For a TI medium, the five wave propagation velocities, i.e., V_{P0}, V_{P45}, V_{P90}, V_{S90} and V_{S0}, are related to the stiffness coefficients. $C_{11} = V_{P90}^2\rho$, $C_{22} = V_{P45}^2\rho$, $C_{33} = V_{P0}^2\rho$, $C_{44} = V_{S90}^2\rho$, and $C_{55} = V_{S0}^2\rho$, where V_{P90} and V_{S90} are the P- and S-

Table 2

Parameters of fracture

Fracture density	Fracture aspect ratio	Fluid density (g/cm^3)	P-wave velocity of fluid (km/s)	S-wave velocity of fluid (km/s)
0.1	0.1	0.9	1.2	0

wave velocities at the horizontal direction, respectively, and V_{P45} is the P-wave velocity at the 45° direction.

3. Forward Modeling Analysis

Based on the theoretical analysis, the forward simulation is performed. First, according to Tables 1 and 2, the influences of fracture parameters on fracture weakness are analyzed. Then, different fracture stiffness matrices are established according to different fracture strikes. The change of stiffness coefficients and velocities regarding fracture strike is analyzed. Finally, by setting the values or ranges of incident angle, azimuth angle, and β, and using the parameters given in Eq. 8 and Table 1, we can obtain the change of P-wave reflection coefficient of model I regarding incident angle and azimuth angle (AVAZ responses). According to the change of reflection coefficients with fracture azimuth, a rose diagram is obtained to analyze the influence of fracture azimuth on the reflection coefficient. Then, the fracture properties are predicted.

3.1. Effects of Fracture Parameters on Fracture Weakness

In fractured reservoirs, the effects of fracture density, fracture aspect ratio, and fluid type on the fracture normal and tangential compliances can be used to characterize the reservoir characteristics to support fracture parameter inversion. The analysis of the influences of different fracture parameters on fracture weakness provides a theoretical basis for the

prediction of fracture density and fluid. The relevant parameters in modeling are given in Table 2.

3.1.1 Effects of Fracture Density

Figure 2 shows fracture weakness versus fracture density for four different fracture aspect ratios. Figure 2a shows that in all four cases there is a linear increase with the increase of fracture density, but the slopes are different. The slope of Δ_N increases with fracture density. In Fig. 2b, Δ_T increases with the increase of fracture density as well; however, it is not affected by the change of fracture aspect ratio. Δ_N is more sensitive to the change of fracture density than Δ_T.

3.1.2 Effects of Fracture Aspect Ratio

Figure 3 shows the effects of fracture aspect ratio on fracture weakness for four different fracture densities. From Fig. 3a, Δ_N increases with the increase of fracture aspect ratio for all cases, and the slope decreases with the increase of fracture aspect ratio. The change of Δ_N becomes more significant when the fracture density increases, and when the fracture density equals to 0.01, Δ_N is almost unchanged. Figure 3b shows that the change of fracture aspect ratio does not affect the tangential weakness of fracture, and it increases with fracture density.

3.1.3 Effects of Fracture-Filling Fluid

Figure 4 shows the effects of fluid density on the fracture weakness regarding the different fluid P-wave velocities. Figure 4a shows that Δ_N decreases with the increase of fluid density or increase of fluid P-wave velocity. As shown in Fig. 4b, Δ_T is not affected by the fluid properties.

3.2. Rock Stiffness Parameters Regarding Fracture Strike

For the analysis of the variation of rock stiffness coefficients regarding fracture strike, the tangential and normal fracture weaknesses in Table 1 are kept
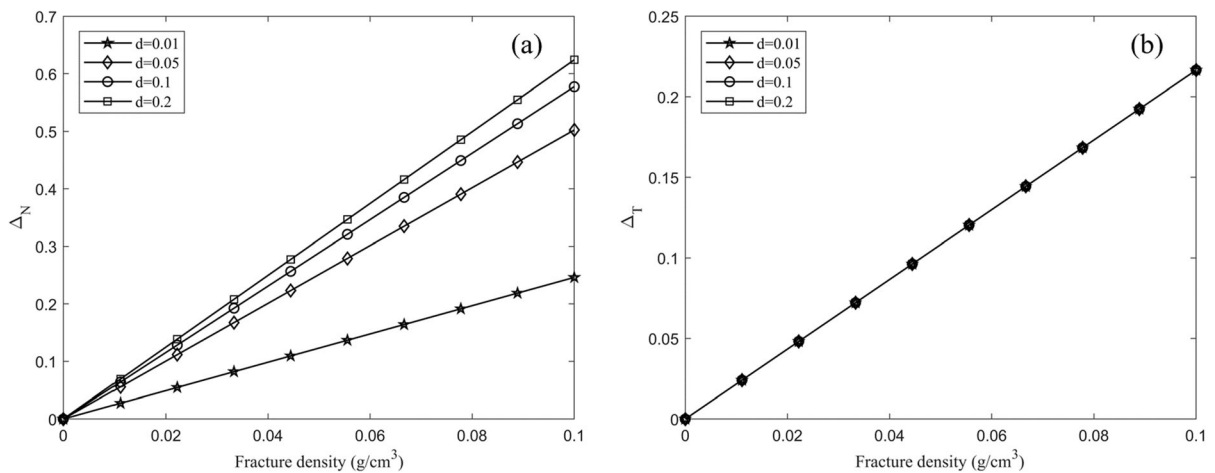
Figure 2
Relation between fracture weakness and fracture density under different aspect ratios. **a** When the aspect ratio of the fracture is 0.01, 0.05, 0.1, or 0.2, the normal fracture weakness changes with the fracture density. **b** When the aspect ratio of the fracture is 0.01, 0.05, 0.1, or 0.2, the fracture tangential weakness changes with the fracture density
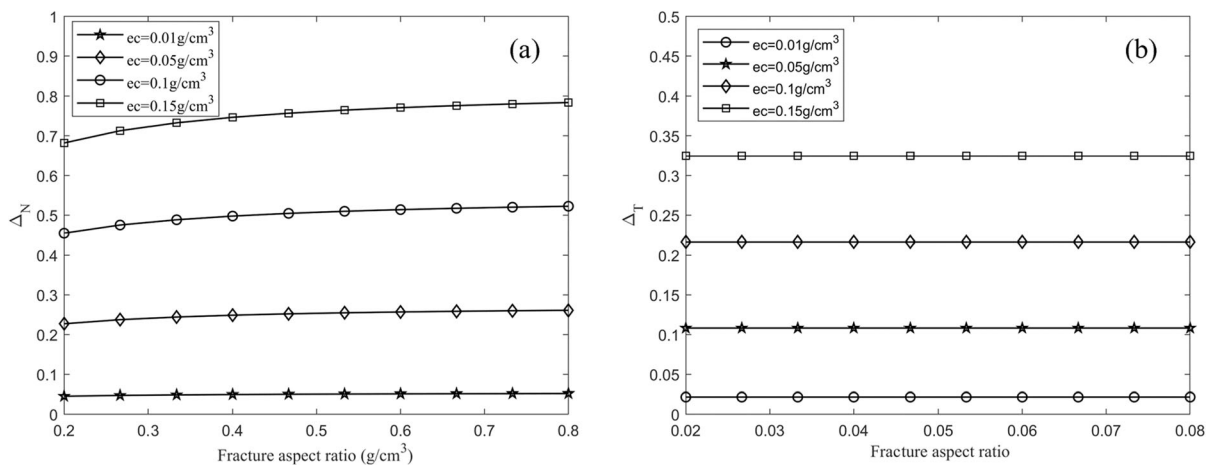

Figure 3
Relation between fracture weakness and fracture aspect ratio under different fracture densities. **a** When the fracture density is 0.01 g/cm^3, 0.05 g/cm^3, 0.1 g/cm^3, or 0.15 cm^3, the relation between the fracture normal weakness and the aspect ratio of fracture. **b** When the fracture density is 0.01 cm^3, 0.05 cm^3, 0.1 cm^3, or 0.15 cm^3, the relation between the fracture tangential weakness and the aspect ratio of fracture

unchanged, and β is changed to obtain the different stiffness matrices. Thus, we obtain the different stiffness coefficients and the relations between the stiffness coefficients and the velocities. By setting β between 0° and 180°, we obtain the variations of stiffness coefficients regarding the fracture orientation as shown in Fig. 5.

We observe that C_{33} does not vary with the fracture strike. As the fracture strike changes, C_{11} and C_{22} fluctuate, and both increase first and then decrease to the minimum in the range from 0° to 90°. The former becomes maximum at 54°, and the latter becomes maximum at 36°. The change in the range from 90° to 180° is symmetrical to that from 0° to 90°. C_{44} increases first and then decreases, while C_{55} has the opposite trend. They are much lower than C_{11}, C_{22} and C_{33}.
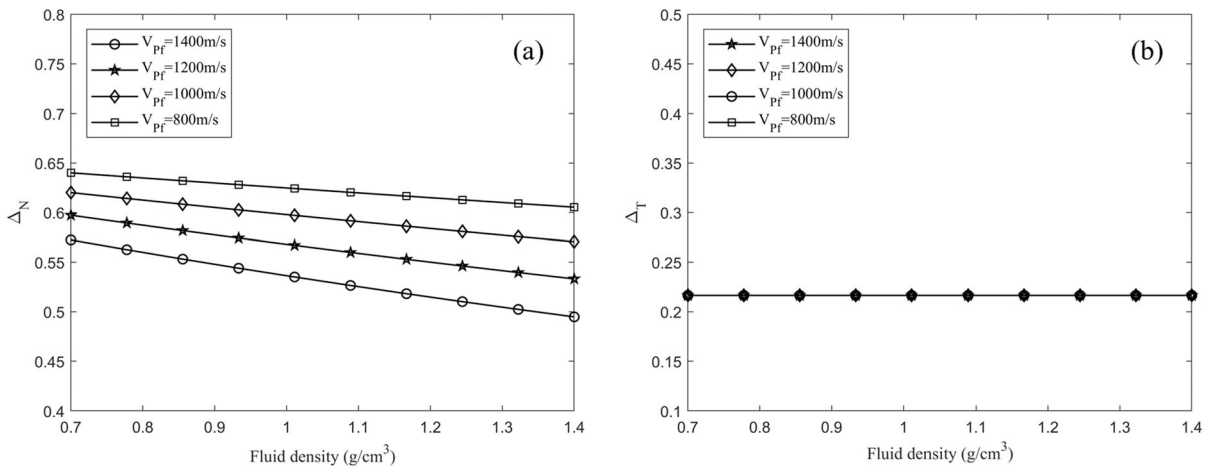
Figure 4

Relation between fracture weakness and fluid density for different P-wave velocities of the fluid. **a** When the P-wave velocity of fluid is 800 m/s, 1000 m/s, 1200 m/s, or 1400 m/s, the fracture normal weakness versus fluid density for variable fluid velocity. **b** When the P-wave velocity of fluid is 800 m/s, 1000 m/s, 1200 m/s, or 1400 m/s, the fracture tangential weakness versus fluid density for variable fluid velocity
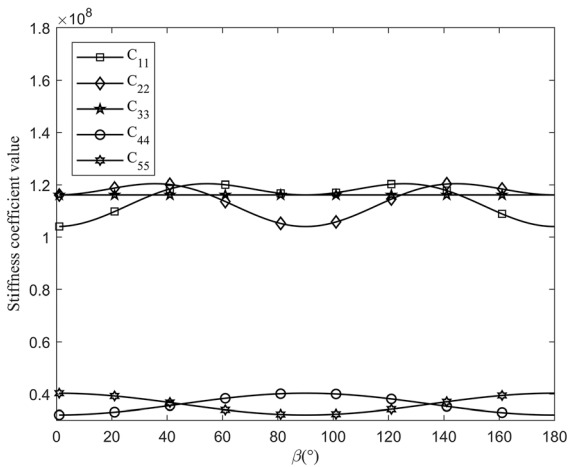

Figure 5

Variation curves of the stiffness coefficients regarding fracture strike
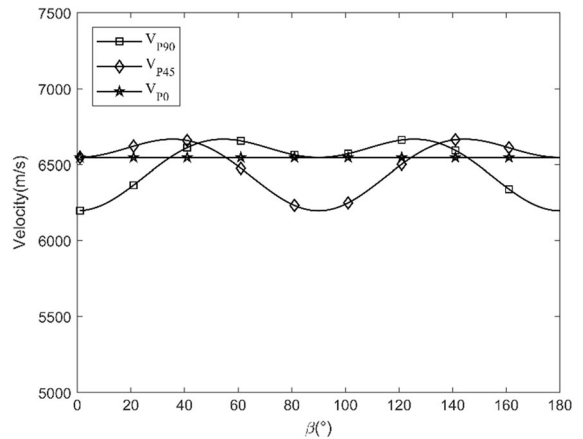
Figure 6

Relation among three P-wave velocities and fracture strike

Based on the equations in Sect. 2.4, three characteristic angle-dependent P-wave velocities are shown in Fig. 6. V_{P0} is a constant of 6547 m/s, and not affected by the fracture strike. V_{P90} is related to the fracture strike and symmetrical at 90°, which increases first and then decreases to a minimum of 6190 m/s in the range from 0° to 90°. V_{P45} also increases first and then decreases from 0° to 90°, but the minimum is 6196 m/s at 0°.

With the equations in Sect. 2.4, two characteristic angle-dependent S-wave velocities are given in Fig. 7 regarding the fracture strike. V_{S90} first decreases and then increases, with the maximum of 3858 m/s at 0° and minimum of 3440 m/s at 90°. When β is set at 0°, V_{S90} is consistent with that in model I. V_{S0} shows an
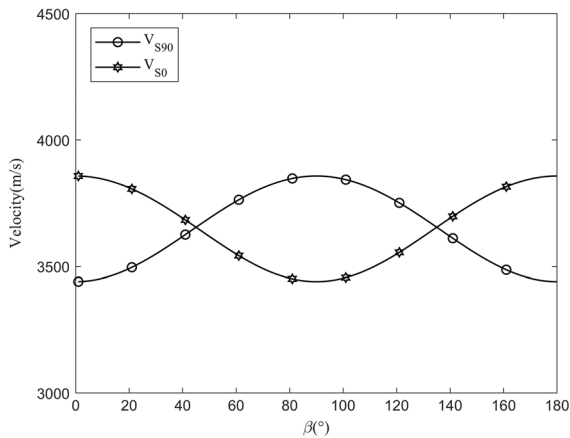
Figure 7
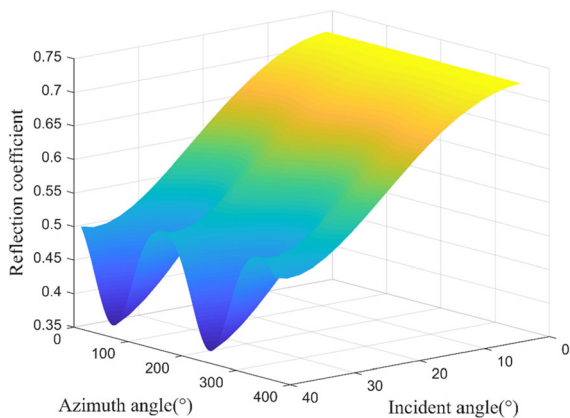Relation between two S-wave velocities and fracture strike

Figure 8
Variation of reflection coefficient regarding incident angle and azimuth angle

opposite trend, and the maximum is 3858 m/s at 90° fracture strike.

3.3. AVAZ Responses with Variable Fracture Azimuth

The incident angle is considered to be between 0° and 40°, and the azimuth angle is considered to be between 0° and 360°. β is set to 30°. We obtain the change of reflection coefficient of model I with incident angle and azimuth angle (AVAZ responses) using Eq. 8 and the parameters given in Table 1. This is shown in Fig. 8. To be more intuitive, the change of the reflection coefficient of model I with azimuth angle is extracted from Fig. 8 when the incident

angles are 10°, 20°, 30°, and 40°. Then, four sets of polar coordinates of reflection coefficient varying with azimuth angle are obtained, as shown in Fig. 9.

In Figs. 8 and 9, the reflection coefficient gradually decreases as the incident angle increases. Furthermore, the variation with azimuth angle is small when the incident angle is small, and the rose diagram is close to a circle, where the azimuthal anisotropy of the reflection coefficient is weak. For a larger incident angle, more significant azimuthal anisotropy is observed. Thus, the P-wave reflection coefficient at the anisotropic interface is related to the incident angle or offset distance.

The long axis of the ellipse for the reflection coefficient can be used to identify the azimuth of fractures. With the fixed incident angle of 40°, and the azimuth of the source-receiver line ϕ (from 0° to 360°), by varying β, the azimuth φ can be obtained, as shown in Fig. 10. The main difference between the seismic AVAZ responses due to fracture disturbance in the HTI model is related to the azimuth variation at large incident angles. The long axis of ellipse indicates fracture strike. When β changes within the range < 90°, the predicted vertical fracture strike varies.

4. Fracture Strike Prediction with Real Seismic Data

The fracture strike estimation with the proposed method is performed on the field seismic data acquired from the work area of Sichuan Basin, southwest China. Figure 11 shows the pre-stack time-migrated AVAZ gathers, which consist of 600 CDPs for 400 lines, with incidence angles of 1°–30° and azimuth angles of 0°–150°. The target fractured shale reservoir is located at about 1700 ms. The solid red line corresponds to the bottom of the target layer, and the seismic horizon of the bottom of the reservoir is shown in Fig. 12.

As is shown in Fig. 12, there is an anticline in the target area due to the lateral tectonic compression. In general, the fractures can be described qualitatively by using waveform-similarity-based attributes, such as the coherent bodies, 3D curvature, ant tracking, and other attribute bodies. Although these properties do not characterize the geometric properties or
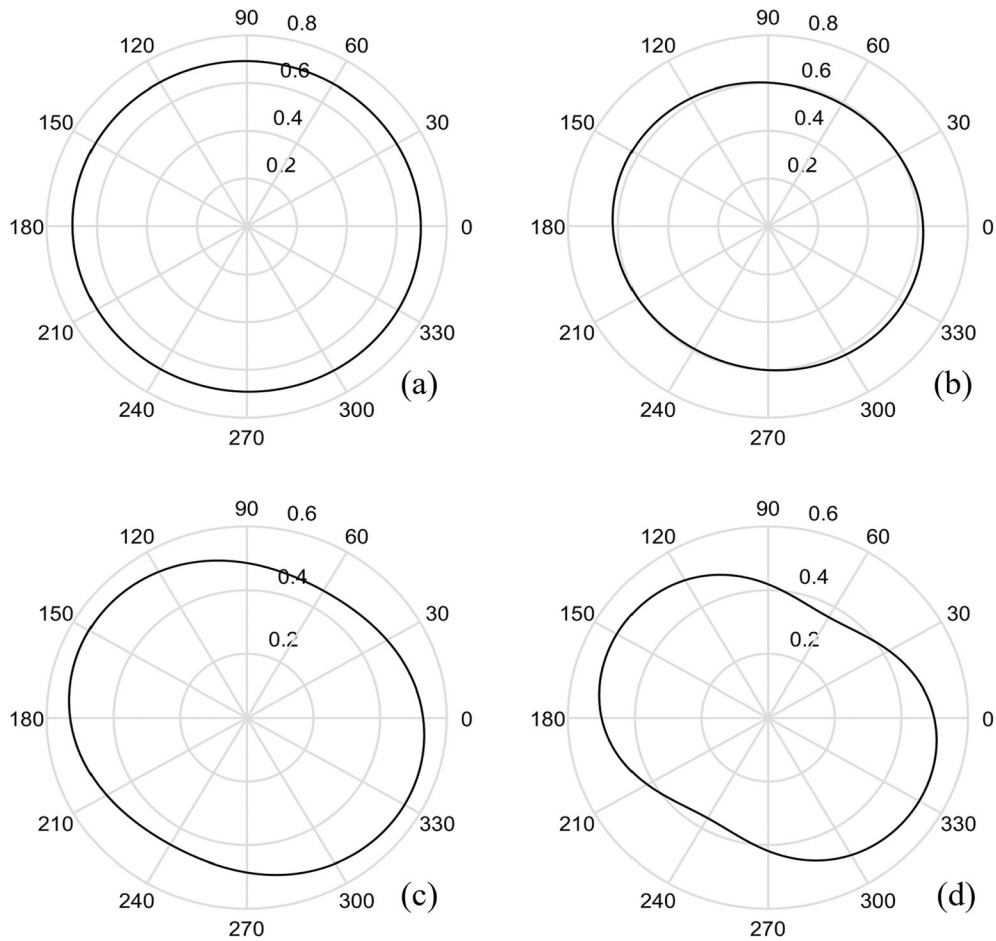
Figure 9
Four groups of reflection coefficients varying with azimuth angle. **a** Rosette with incident angle of 10° and reflection coefficient changing with azimuth angle. **b** Rosette with incident angle of 20° and reflection coefficient changing with azimuth angle. **c** Rosette with incident angle of 30° and reflection coefficient changing with azimuth angle. **d** Rosette with incident angle of 40° and reflection coefficient changing with azimuth angle

orientations of the fractures, they can be used to approximately describe the spatial distribution of fractures. Figure 13 shows the ant-tracking attribute of the target area following a previously presented method (Randen et al., 2001; Pedersen et al., 2002, 2003; Zhao et al., 2018). It indicates many fractures in the target area, especially around the anticline location. The red solid curves in Fig. 12 indicate anticline location. Comparing Figs. 12 and 13 shows that many fractures are developed at the locations around two flanks of the anticline.

In the following, we neglect the lateral variations of the fracture dip angle and assume that all the fractures are vertical fractures since they are mostly high-angle fractures in the target area. This is consistent with the assumptions of rock physical modeling in this work, so the proposed model is applied to perform the fracture strike estimation.

Based on the analysis, the long axis of the rosettes of AVAZ gathers corresponds to the strike of fractures. It provides the possibility to use AVAZ seismic data to estimate the strike. The rosettes of seismic data are produced in the vicinity of the target layer corresponding to the red curves in Fig. 11, and the rosettes are given in Fig. 14.

To improve the signal-to-noise ratio, we consider the partially stacked data in ranges of 0–10°, 10–20°, and 20–30° as the near-, medium- and far-angle
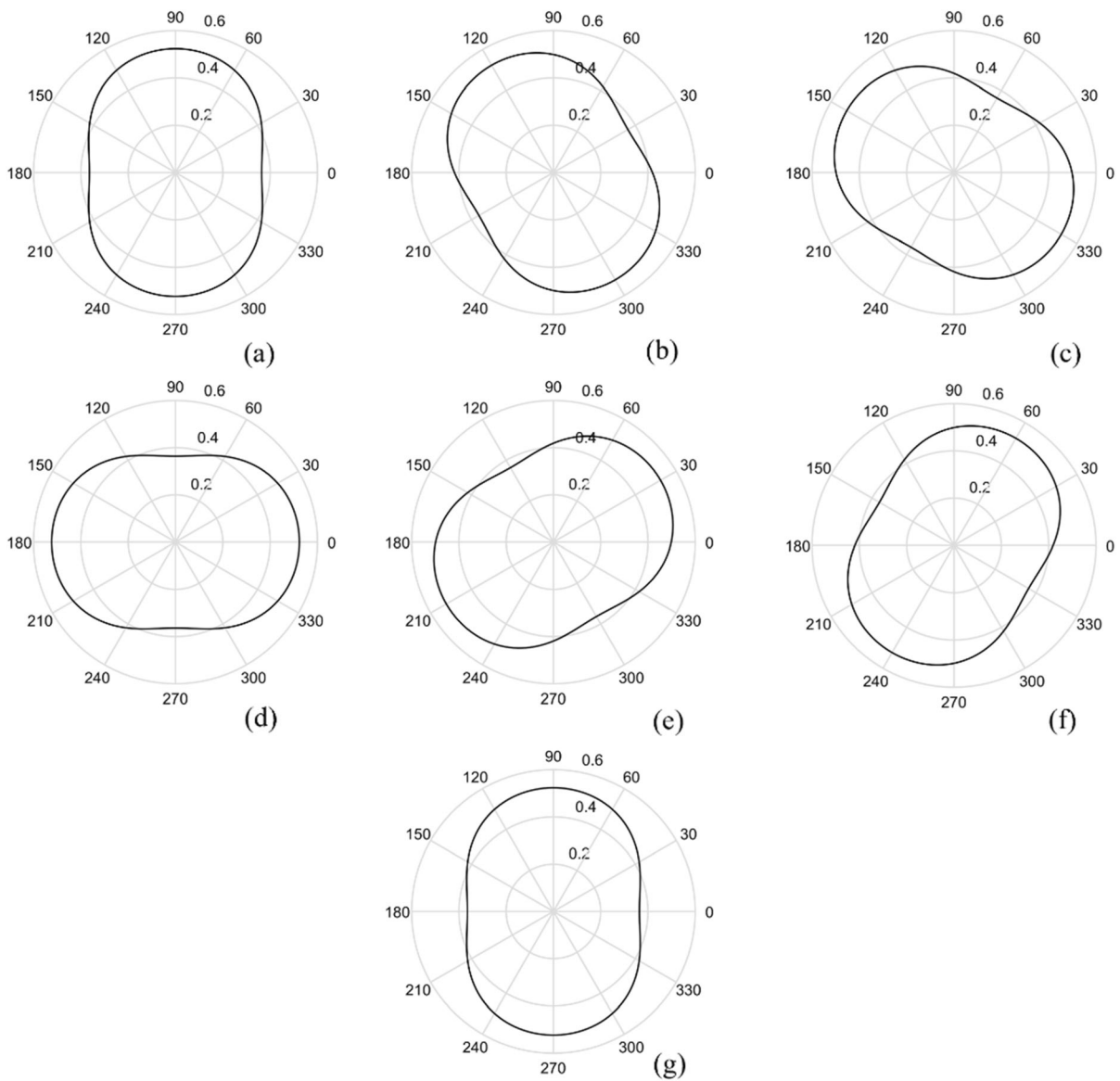
Figure 10
AVAZ responses with variable azimuth. **a** AVAZ response with variable azimuth angle when β is 0°. **b** AVAZ response with variable azimuth angle when β is 15°.**c** AVAZ response with variable azimuth angle when β is 30°.**d** AVAZ response with variable azimuth angle when β is 45°.**e** AVAZ response with variable azimuth angle when β is 60°.**f** AVAZ response with variable azimuth angle when β is 75°.g AVAZ response with variable azimuth angle when β is 90°

incidence data, respectively. Figure 14 shows that the fracture strikes are majorly distributed at around 200°. Figure 15 also shows the estimated maximum horizontal principal stress, which is estimated by using the method presented by Li et al. (2022). Similarly, we analyze the seismic data at the target

layer for the entire work and estimate the fracture strikes. The arrows in Fig. 15 correspond to the fracture directions within the target layer. The directions of faults and fracture developments are generally along the northeast direction.
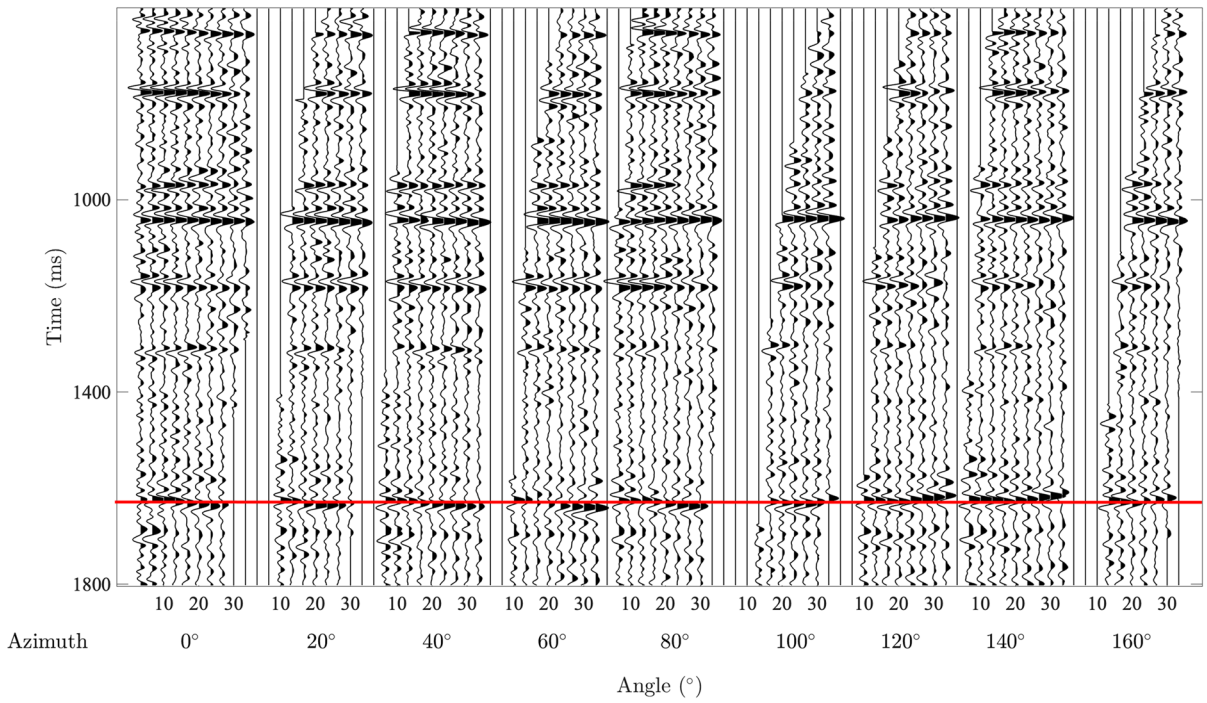
Figure 11
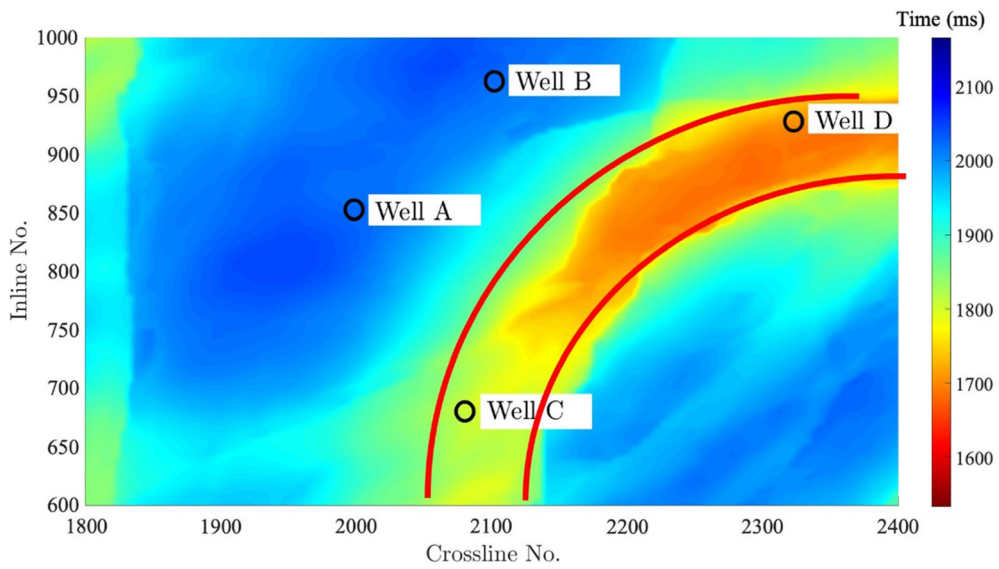Pre-stack azimuthal angle gathers of seismic data with the target horizon bottom indicated by red line

Figure 12
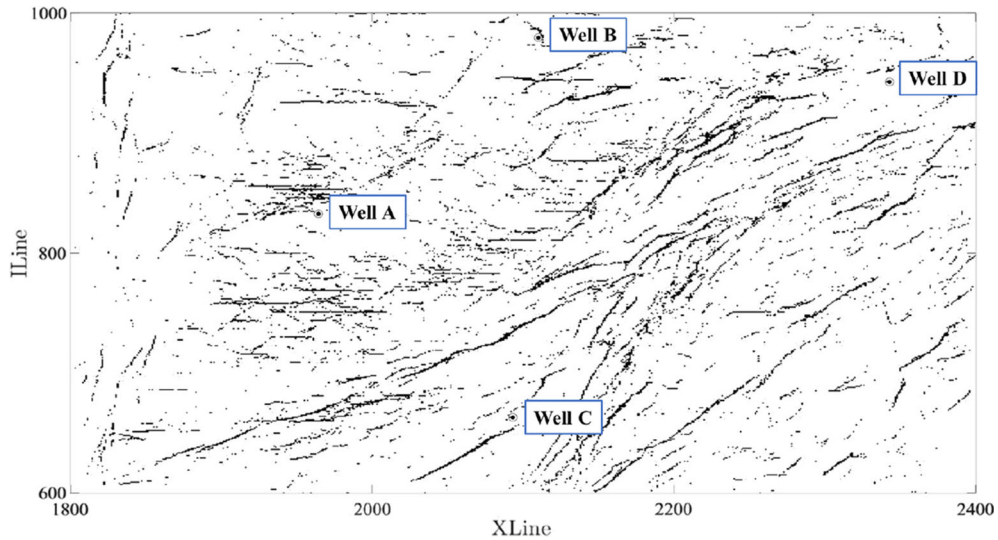Three-dimensional depth domain seismic horizon of the reservoir bottom

Figure 13
Ant-tracking attribute of the target area

To verify the validity of the proposed method, we compare the interpretation results on the basis of well-bore imaging logs with the predicted fracture strikes. Well B with the black dashed box in Fig. 15 is considered for the comparative analysis.

Figure 16 shows (a) bulk and (b) shear moduli, (c) density, (d) normal and (e) tangential fracture weaknesses, (f) fracture density, (g) fracture filling fluid indicator $1/F$c, (h) differential horizontal stress ratio (DHSR), (i) fracture strike, and (j) volume contents of minerals, with (Huang et al., 2022)

$$F_C = 1 - \zeta^b + \frac{K'}{\pi \mu^b \chi},   (15)$$

and

$$\text{DHSR} = \frac{\sigma_H - \sigma_h}{\sigma_H},   (16)$$

where ζ^b denotes shear modulus, σ_H is maximum horizontal principal stress, and σ_h is minimum horizontal principal stress. The areas with a high fracture density, high DHSR, and high $1/F$c (at around 2.4–2.42 s) indicate high-quality gas-bearing fractured reservoirs.

The fracture strikes interpretated based on the well-bore imaging logs are given in Fig. 16i, which shows that the fractures are developed along the northeast direction. We highlight the seismic estimation results corresponding to well B (black dashed box), which is in good agreement with the results of well-bore imaging logs.
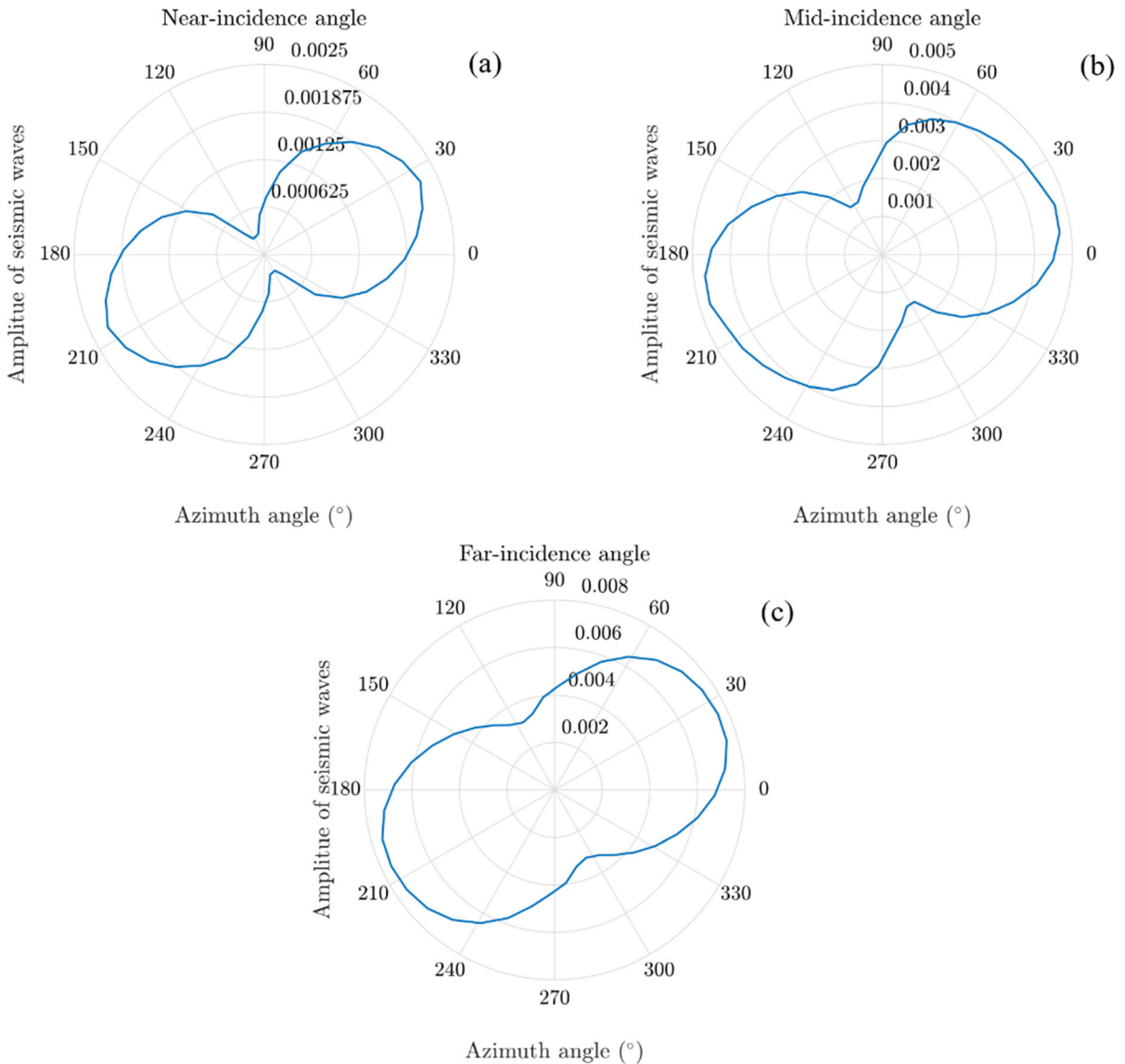
Figure 14
Rosette diagrams based on the real seismic data

5. Conclusion

Traditional seismic fracture strike prediction method is based on the Rüger approximation to analyze and invert fracture-related parameters. In this work, a fracture strike estimation method is proposed based on the Schoenberg linear slip model and scattering theory. We derive the stiffness matrix by introducing a set of fractures with different strikes into the host matrix. Based on the scattering theory of Shaw and Sen (2006), the P–P wave reflection of the fractured model is modeled. When a P-wave propagates in an HTI medium, the P-wave reflection coefficient regarding azimuth can be approximately described with an ellipse, and the long axis of the ellipse may indicate the direction of fracture. The proposed fracture strike prediction method achieves the satisfactory results for estimating the fracture
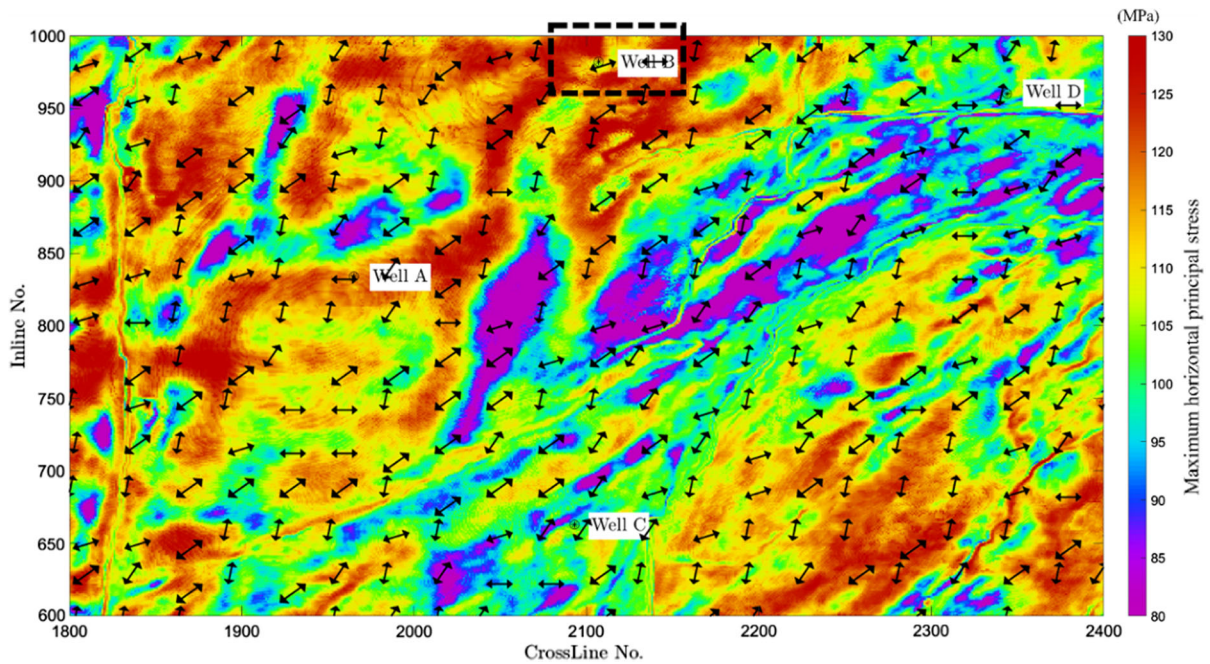
Figure 15
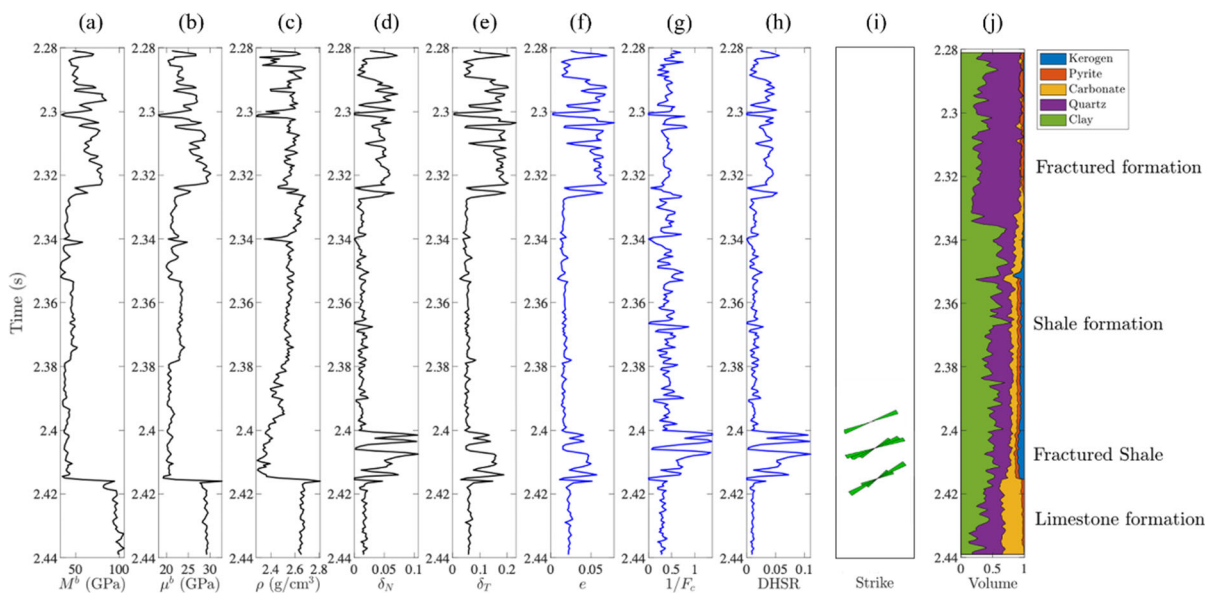Fracture strike estimation by using the proposed method and maximum horizontal principal stress

Figure 16
Fracture strike interpretated by the well-bore imaging. **a** Variation of fracture bulk modulus with time. **b** Variation of fracture shear modulus with time. **c** Variation of density with time. **d** Variation of fracture normal weakness with time. **e** Variation of fracture tangential weakness with time. **f** Variation of fracture density with time, **g** fracture filling fluid indicator $1/F_c$. **h** Variation of differential horizontal stress ratio with time. **i** Interpretation of fracture strike by well-bore imaging. **j** Variation of volume content of various minerals with time

strikes with the seismic data from the work area of Sichuan Basin, and the predictions are consistent with the well-bore imaging results. The application indicates that the proposed method is feasible for predicting the fracture strikes in the complex HTI formations.

Author Contributions JB: supervision, modeling, writing-reviewing and funding acquisition. WZ: methodology, modeling, writing and draft preparation. GH: software, validation, editing and writing. TMM: writing-reviewing and suggestion. CL: writing-reviewing. All authors contributed to the article and approved the submitted version.

Data Availability

The data can be accessed by contacting the corresponding author.

Declarations

Conflict of Interest The authors declare no competing interests.*Appendix A: Calculation formulas of ξ and η in Eq. 6*

$$t = [\sin\theta\cos\varphi, \sin\theta\sin\varphi, \cos\theta], \quad (A-1a)$$

$$\mathbf{t}' = [-\sin\theta\cos\varphi, \sin\theta\sin\varphi, \cos\theta], \quad (A-1b)$$

$$\mathbf{p} = \frac{1}{\alpha_b}[\sin\theta\cos\varphi, \sin\theta\sin\varphi, \cos\theta], \quad (A-1c)$$

$$\mathbf{p}' = \frac{1}{\alpha_b}[-\sin\theta\cos\varphi, -\sin\theta\sin\varphi, \cos\theta], \quad (A-1d)$$

$$\xi = \mathbf{t}_i\mathbf{t}_i' = \cos^2\theta - \sin^2\theta = \cos 2\theta, \quad (A-2a)$$

$$\eta_{mn} = \mathbf{t}_i'\mathbf{p}_j'\mathbf{t}_k\mathbf{p}_l, \quad (A-2b)$$

where the corresponding parameters η_{mn} are determined.

$$\eta_{11} = \sin^4\theta\cos^4\varphi / a_b^2, \quad (A-3a)$$

$$\eta_{12} = \sin^4\theta\sin^2\varphi\cos^2\varphi / a_b^2, \quad (A-3b)$$

$$\eta_{13} = \sin^2\theta\cos^2\theta\cos^2\varphi / a_b^2, \quad (A-3c)$$

$$\eta_{14} = 2\sin^3\theta\cos\theta\sin\varphi\cos^2\varphi / \alpha_b^2, \quad (A-3d)$$

$$\eta_{15} = -2\sin^3\theta\cos\theta\cos^3\varphi / a_b^2, \quad (A-3e)$$

$$\eta_{16} = 2(\sin^4\theta\sin\varphi\cos^3\varphi) / a_b^2, \quad (A-3f)$$

$$\eta_{22} = \sin^4\theta\sin^4\varphi / a_b^2, \quad (A-3g)$$

$$\eta_{23} = \sin^2\theta\cos^2\theta\sin^2\varphi / a_b^2, \quad (A-3h)$$

$$\eta_{24} = -2\sin^3\theta\cos\theta\sin^3\varphi / a_b^2, \quad (A-3i)$$

$$\eta_{25} = -2\sin^3\theta\cos\theta\sin^2\varphi\cos\varphi / a_b^2, \quad (A-3j)$$

$$\eta_{26} = 2(\sin^4\theta\sin^3\varphi\cos\varphi) / a_b^2, \quad (A-3k)$$

$$\eta_{33} = \cos^4\theta / a_b^2, \quad (A-3l)$$

$$\eta_{34} = 2\sin\theta\cos^3\theta\sin\varphi / a_b^2, \quad (A-3m)$$

$$\eta_{35} = -2\sin\theta\cos^3\theta\cos\varphi / a_b^2, \quad (A-3n)$$

$$\eta_{36} = 2(\sin^2\theta\cos^2\theta\sin\varphi\cos\varphi) / a_b^2, \quad (A-3o)$$

$$\eta_{44} = -4\sin^2\theta\cos^2\theta\sin^2\varphi / a_b^2, \quad (A-3p)$$

$$\eta_{45} = -4\sin^2\theta\cos^2\theta\sin\varphi\cos\varphi / a_b^2, \quad (A-3q)$$

$$\eta_{46} = -4\sin^3\theta\cos\theta\sin^2\varphi\cos\varphi / a_b^2, \quad (A-3r)$$

$$\eta_{55} = -4\sin^2\theta\cos^2\theta\cos^2\varphi / a_b^2, \quad (A-3s)$$

$$\eta_{56} = -4\sin^3\theta\cos\theta\sin\varphi\cos^2\varphi / a_b^2, \quad (A-3t)$$

$$\eta_{66} = 4\sin^4\theta\sin^2\varphi\cos^2\varphi / a_b^2, \quad (A-3u)$$

and

$$\eta_{21} = \eta_{12}, \quad (A-4a)$$

$$\eta_{31} = \eta_{13}, \quad (A-4b)$$

$$\eta_{32} = \eta_{23}, \quad (A-4c)$$

$$\eta_{41} = \eta_{14}, \quad (A-4d)$$

$$\eta_{42} = \eta_{24}, \quad (A-4e)$$

$$\eta_{43} = \eta_{34}, \qquad (A-4f)$$

$$\eta_{51} = \eta_{15}, \qquad (A-4g)$$

$$\eta_{52} = \eta_{25}, \qquad (A-4h)$$

$$\eta_{53} = \eta_{35}, \qquad (A-4i)$$

$$\eta_{54} = \eta_{45}, \qquad (A-4j)$$

$$\eta_{61} = \eta_{16}, \qquad (A-4k)$$

$$\eta_{62} = \eta_{26}, \qquad (A-4l)$$

$$\eta_{63} = \eta_{36}, \qquad (A-4m)$$

$$\eta_{64} = \eta_{46}, \qquad (A-4n)$$

$$\eta_{65} = \eta_{56}, \qquad (A-4o)$$

where a_b represents the P-wave velocity of the host medium. and φ denotes the azimuth angle.

REFERENCES

Afzal, D. M. Z., Atif, R. S., Maryam, T., Ghulam, S., & Bakhtawer, S. (2022). Characterization of seismic anisotropy using azimuthal AVO analysis (AVAz)—An application case study in the deep and tight carbonate reservoirs from Potwar Basin onshore Pakistan. *Journal of Applied Geophysics, 205*(1), 104767. https://doi.org/10.1016/J.JAPPGEO.2022.104767

Al-Marzoug, A. M. (2006). P-wave anisotropy from azimuthal AVO and velocity estimates using 3D seismic data from Saudi Arabia. *Geophysics, 71*(2), E7–E11. https://doi.org/10.1190/1.2187724

Bachrach, R., Sengupta, M., Salama, A., & Miller, P. (2009). Reconstruction of the layer anisotropic elastic parameter and high-resolution fracture characterization from P-wave data: A case study using seismic inversion and Bayesian rock physics parameter estimation. *Geophysical Prospecting, 57*(2), 253–262. https://doi.org/10.1111/j.1365-2478.2008.00768.x

Bahorich, M., & Farmer, S. (1995). 3-D seismic discontinuity for faults and stratigraphic features: The coherence cube. *SEG Technical Program Expanded Abstracts, 14*(10), 1053–1058. https://doi.org/10.1190/1.1887523

Chopra, S., & Marfurt, K. J. (2007). Curvature attribute applications to 3D surface seismic data. *The Leading Edge, 26*(4), 404–414. https://doi.org/10.1190/1.2723201

Crampin, S. (1981). A review of wave motion in anisotropic and cracked elastic-media. *Wave Motion, 3*(4), 343–391. https://doi.org/10.1016/0165-2125(81)90026-3

Crampin, S. (1985). Evaluation of anisotropy by shear-wave splitting. *Geophysics, 50*(1), 142–152. https://doi.org/10.1190/1.1441824

Dorigo, M., Maniezzo, V., & Colorni, A. (1996). Ant system: Optimization by a colony of cooperating agents. *IEEE Transactions on Systems Man and Cybernetics (part B), 26*(1), 29–41. https://doi.org/10.1109/3477.484436

Downton, J., & Roure, B. (2010). Azimuthal simultaneous elastic inversion for fracture detection. *SEG Technical Program Expanded Abstracts, 29*, 263–267. https://doi.org/10.1190/1.3513389

Downton, J., & Roure, B. (2015). Interpreting azimuthal Fourier coefficients for anisotropic and fracture parameters. *Interpretation, 3*(3), ST9-ST27. https://doi.org/10.1190/INT-2014-0235.1

Gong, L., Gao, S., Liu, B., Yang, J., Fu, X., Xiao, F., et al. (2021a). Quantitative prediction of natural fractures in shale oil reservoirs. *Geofluids, 2021*(3), 1–15. https://doi.org/10.1155/2021/5571855

Gong, L., Wang, J., Gao, S., Fu, X., Liu, B., Miao, F., et al. (2021b). Characterization, controlling factors and evolution of fracture effectiveness in shale oil reservoirs. *Journal of Petroleum Science and Engineering, 203*(2), 108655. https://doi.org/10.1016/j.petrol.2021b.108655

Hsu, C. J., & Schoenberg, M. (1993). Elastic waves through a simulated fractured medium. *Geophysics, 58*(7), 964–977. https://doi.org/10.1190/1.1443487

Huang, G., Ba, J., Gei Davide, M., & Jose, Carcione. (2022). A matrix-fracture-fluid decoupled PP reflection coefficient approximation for seismic inversion in tilted transversely isotropic media. *Geophysics, 87*(6), 275–292. https://doi.org/10.1190/GEO2021-0631.1

Hudson, J. A. (1981). Wave speeds and attenuation of elastic waves in material containing cracks. *Geophysical Journal International, 64*(1), 133–150. https://doi.org/10.1111/j.1365-246X.1981.tb02662.x

Li, T. (1999). Fracture signatures on P-wave AVOZ. *SEG Technical Program Expanded Abstracts, 15*(1), 1818–1821. https://doi.org/10.1190/1.1826490

Li, L., Guo, Y., Zhang, X., Pan, X., Zhang, J., & Lin, Y. (2022). Seismic characterization of in situ stress in orthorhombic shale reservoirs using anisotropic extended elastic impedance inversion. *Geophysics, 87*(6), 1–68. https://doi.org/10.1190/geo2021-0807.1

Li, Y. W., Sun, W., Liu, X., Zhang, D., Wang, Y., & Liu, Z. (2018). Study of the relationship between fractures and highly productive shale gas zones, Longmaxi Formation, Jiaoshiba area in eastern Sichuan. *Petroleum Science, 15*(3), 498–509. https://doi.org/10.1007/s12182-018-0249-7

Lisle, R. J. (1994). Detection of zones of abnormal strains in structures using Gaussian curvature analysis. *AAPG Bulletin, 1994*(78), 1811–1819. https://doi.org/10.1306/A25FF305-171B-11D7-8645000102C1865D

Liu, X., Guo, Z., & Han, X. (2018a). Full waveform seismic AVAZ signatures of anisotropic shales by integrated rock physics and the reflectivity method. *Journal of Geophysics and Engineering*. https://doi.org/10.1088/1742-2140/aaa3d3

Liu, Y., Liu, X., Lu, Y., Chen, Y., & Liu, Z. (2018b). Fracture prediction approach for oil- bearing reservoir based on AVAZ attributes in orthorhombic medium. *Petroleum Science, 15*(3), 510–520. https://doi.org/10.1007/s12182-018-0250-1

Liu, Y., Zhu, Z., Pan, R., Gao, B., & Jin, J. (2022). Analysis of AVAZ seismic forward modeling of fracture-cavity reservoirs of the dengying formation, Central Sichuan Basin. *Energies, 15*(14), 5022. https://doi.org/10.3390/EN15145022

Long, P., Zhang, J., & Tang, X. (2011). Feature of muddy shale fissure and its effect for shale gas exploration and development. *Natural Gas Geoscience, 22*(3), 525–532.

Lyu, W., Zeng, L., Zhang, B., Miao, F., Lyu, P., & Dong, S. (2017). Influence of natural fractures on gas accumulation in the Upper Triassic tight gas sandstones in the northwestern Sichuan Basin, China. *Marine and Petroleum Geology, 83*, 60–72. https://doi.org/10.1016/j.marpetgeo.2017.03.004

Mallick, S., Craft, K. L., Meister, L. J., & Chambers, R. E. (1998). Determination of the principal directions of azimuthal anisotropy from P-wave seismic data. *Geophysics, 63*, 692–706. https://doi.org/10.1190/1.1444369

Marfurt, K. J., Kirlin, R. L., Farmer, S. L., et al. (1998). 3-D seismic attributes using a emblance-based coherency algorithm. *Geophysics, 63*(4), 1150–1165.

Pan, B., Mrinal, K. S., & Gu, H. (2016). Joint inversion of PP and PS AVAZ data to estimate the fluid indicator in HTI medium: A case study in Western Sichuan Basin, China. *Journal of Geophysics and Engineering*. https://doi.org/10.1088/1742-2132/13/5/690

Pan, X., Zhang, G., Chen, H., & Yin, X. (2017). McMC-based AVAZ direct inversion for fracture weaknesses. *Journal of Applied Geophysics*. https://doi.org/10.1016/j.jappgeo.2017.01.015

Penersen, S. I., & Skov, T. (2002). Automatic fault extraction using artificial ants. *SEG Technical Program Expanded Abstracts, 21*, 512–515. https://doi.org/10.1190/1.1817297

Pedersen, S. I., Skov, T., Hetlelid, A., Fayemendy, P., Ramden, T. & Sonneland, L. (2003). *New paradigm of fault interpretation: 73rd Annual International meeting SEG Technical Program Expanded Abstracts: Society of Exploration Geophysicists*, pp 350–353.

Randen, T., Pedersen, S. I., & Snneland, L. (2001). *Automatic detection and extraction of faults from three-dimensional seismic data: 71st Annual International meeting SEG Technical Program Expanded Abstracts: Society of Exploration Geophysicists*, pp 551–555.

Rüger, A. (1998). Variation of P-wave reflectivity with offset and azimuth in anisotropic media. *Geophysics, 63*(3), 935–947. https://doi.org/10.1190/1.1444405

Rüger, A. (2002). Reflection coefficients and azimuthal AVO analysis in anisotropic media. *Society of Exploration Geophysicists*. https://doi.org/10.1190/1.9781560801764

Sayers, C. M., & Dean, S. (2001). Azimuth-dependent AVO in reservoirs containing non-orthogonal fracture sets. *Geophysical Prospecting, 49*(1), 100–106. https://doi.org/10.1046/j.1365-2478.2001.00236.x

Schoenberg, M. (1980). Elastic wave behavior across linear slip interfaces. *The Journal of the Acoustical Society of America, 68*(5), 1516–1521. https://doi.org/10.1121/1.385077

Schoenberg, M., Dean, S., & Sayers, C. M. (1999). Azimuth-dependent tuning of seismic waves reflected from fractured reservoirs. *Geophysics, 64*(4), 1160–1171. https://doi.org/10.1190/1.1444623

Schoenberg, M., & Douma, J. (1988). Elastic wave propagation in media with parallel fractures and aligned cracks. *Geophysical Prospecting, 36*(6), 571–590. https://doi.org/10.1111/j.1365-2478.1988.tb02181.x

Schoenberg, M., & Sayers, C. M. (1995). Seismic anisotropy of fractured rock. *Geophysics, 60*, 204–211. https://doi.org/10.1190/1.1443748

Shaw, R. K., & Sen, M. K. (2004). Born integral, Stationary phase and linearized reflection coefficients in weak anisotropic media. *Geophysical Journal International, 158*(1), 225–238. https://doi.org/10.1111/j.1365-246X.2004.02283.x

Shaw, R. K., & Sen, M. K. (2006). Use of AVOA data to estimate fluid indicator in a vertically fractured medium. *Geophysics, 71*(3), C15–C24. https://doi.org/10.1190/1.2194896

Teng, L. (1998). *Seismic and rock-physics characterization of fractured reservoirs*. Stanford University.

Thomsen, L. (1986). Weak elastic anisotropy. *Geophysics, 51*(10), 1954–1966. https://doi.org/10.1190/1.1442051

Wang, J., Zhang, J., & Wu, G. (2021). Wide-azimuth Young's modulus inversion and fracture prediction: An example of H structure in Bozhong sag. *Oil Geophysical Prospecting, 56*(3), 593–602.

Yin, X., Liu, Z., Li, C., Li, A., & Gai, H. (2014). Fracture formation prediction with a steady azimuth AVO gradient unconstrained inversion method. *Geophysical Prospecting for Petroleum, 53*(6), 683–691. https://doi.org/10.3969/j.issn.1000-1441.2014.06.008

Zhao W., Sun, D., Zhang, T., Lin, Y., Bie, J., & Li, J. (2018). Application of improved ant-tracking method in carbonate-fracture reservoir. In: *88th Annual International meeting SEG Technical Program Expanded Abstracts: Society of Exploration Geophysicists*, pp 1633–1638. https://doi.org/10.1190/segam2018-2997357.1